Force decomposition and toughness estimation from puncture experiments in soft solids

Pranav Shrestha[1]*, Curtis Geffner[1], Matthew Jaffey[1], Zhongnan Wu[1], Martina Iapichino[1], Mattia Bacca[1], Boris Stoeber[1,2]*

[1] Department of Mechanical Engineering, The University of British Columbia, 2054-6250 Applied Science Lane, Vancouver, British Columbia, V6T 1Z4, Canada.

[2] Department of Electrical and Computer Engineering, The University of British Columbia, 2332 Main Mall, Vancouver, British Columbia, V6T 1Z4, Canada.

* Corresponding authors (email: pranav.shrestha@alumni.ubc.ca, boris.stoeber@ubc.ca)

Table of Contents

Soft solid specimen fabrication and preparation

PDMS is widely used for a variety of biological and medical applications, including those involving soft lithography of micro or nano-fabricated structures and devices, due to its biocompatibility, chemical inertness and thermal stability[1–3]. The following steps are used to prepare the soft solid for the experiments from polydimethylsiloxane (PDMS), SYLGARD 184 Silicone Elastomer, Dow. :

1. *Preparation of sacrificial layer*: Polyacrylic acid (PAA) serves as a sacrificial layer to allow for easy removal of the PDMS after curing. PAA is mixed with deionized or distilled water in a vortex mixer to create a 20% (w/w) PAA solution. The mixed solution is passed through a 0.45 μm filter to remove any particles.

2. *Coating sacrificial layer*: The sacrificial layer, 20% PAA solution, is poured on a glass petri dish that has been plasma cleaned (Plasma Cleaner, Harrick Plasma) to allow for better adhesion. The water is evaporated from the solution by placing the glass petri dish on a hot plate at 150 ˚C for 5 minutes.

3. *Mixing PDMS*: PDMS is prepared by mixing the base and curing agent at a 30:1 weight ratio in a centrifugal mixer (Thinky ARE-310 Centrifugal Mixer, Thinky USA Inc.) at 2000 rpm for 2.5 minutes, and defoaming for 30 seconds at 2200 rpm.

4. *Pour and degas PDMS*: A fixed weight of the PDMS (to produce a resulting height of around 4 mm) is poured on the glass petri dish (coated with sacrificial layer) and the petri dish is placed in a vacuum chamber for around 30 minutes to remove any air bubbles created during the mixing or pouring processes.

5. *Curing PDMS*: The glass petri dish with the PDMS is placed in an oven at 60˚C for around 12 hours to cure and crosslink the PDMS.

6. *Peeling PDMS layer*: After the PDMS has solidified, the sacrificial layer is dissolved in water and the PDMS is peeled off the glass petri dish.

7. *Surface coating*: Carbon Black (VULCAN XC72R Specialty Carbon Black, Cabot Corporation) is applied to the top surface of the PDMS with a cotton swab to visualize the surface during needle insertion and enable detection of puncture initiation during high-speed imaging. The carbon black particles are applied to the center of the sample prior to cutting (next step) to prevent the particles from electrostatically adhering to the side surfaces of the sample and interfering with image clarity. To further minimize the risk of carbon black marking the sample sides, any loose carbon black particles are gently wiped away from the surface of the PDMS with a clean cotton swab.

8. *Sample cutting*: The 4 mm thick PDMS is cut in 10 mm by 10 mm squares (Fig. S1a), and each cut occurs with a single stroke of a sharp, flat-edged knife (*e.g.* #18 X-Acto blade). The sample size is sufficiently large (with the sides approximately 50 times larger than the outer diameter of the needle) to avoid edge effects and to minimize warping of the sides during insertion. Square samples prevent glare from the front-illumination, while circular cuts made with hole punches were found to create glare that interfere with imaging. Additionally, the 10 mm by 10 mm square samples are sufficiently large to minimize warping-induced-glare even for softer PDMS (40:1 mixing ratio; with elastic modulus of 50 kPa) and larger needles (up to 23 G). In this study, 33 gauge (33G) hypodermic needles (Fig. S1d) are inserted into the 10 × 10mm PDMS samples made with 30:1 mixing ratio.
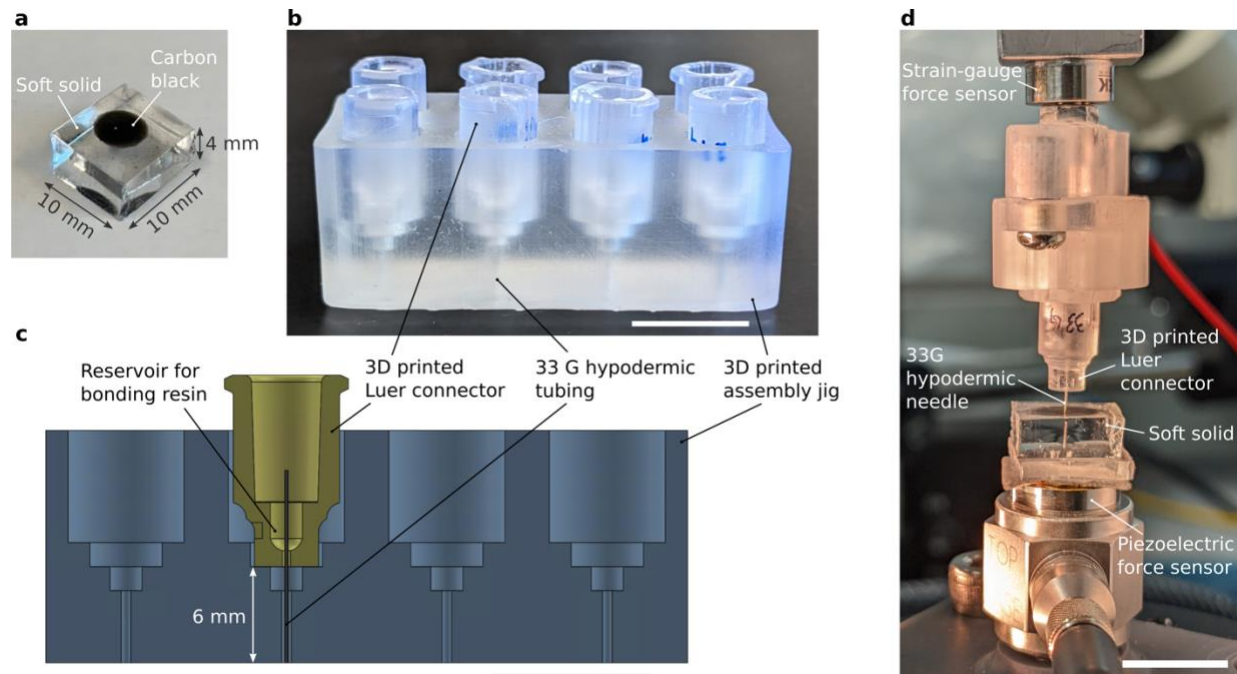
Figure S1 Soft solid and needle-Luer assembly: a) Example of soft solid sample made out of transparent PDMS (30:1 mixing ratio of base to curing agent) with carbon black coating on the top surface, and hole near the center after insertion and re-insertion experiments. b) A 3D printed assembly jig is used to align and assemble eight 3D printed Luer connectors with eight hypodermic tubing, bonding them using UV-curable resin. c) Cross-section of the 3D printed assembly jig showing one Luer connector and a 33G hypodermic needle (12 mm long, with exposed or target needle height of 6 mm after assembly). d) Setup during low-speed insertion of 33G needle into soft solid; Scale bars in b, c, and d are 10 mm.

Soft solid specimen mechanical properties

Compression tests are performed using the Bose ElectroForce 3100 Test Instrument. A 10 mm punching tool is used to punch circular samples for the test. The force and displacement data from the Bose ElectroForce 3100 Test Instrument are used to calculate the compressive stress and strain, accounting for the lateral expansion of the sample during compression (using a Poisson's ratio of 0.5). The slope of a line of best fit up to a compressive strain of 0.1 yields the elastic or Young's modulus for the samples (Figure S2). Table S1 shows the values for Young's modulus, R^2 fit for the slope, average sample thickness and average sample diameter for 3 types of samples: using 30:1 mixing ratio, 40:1 mixing ratio, and a tri-layer PDMS using different mixing ratios.

Table S1: Summary of mechanical properties and geometries of different testing samples

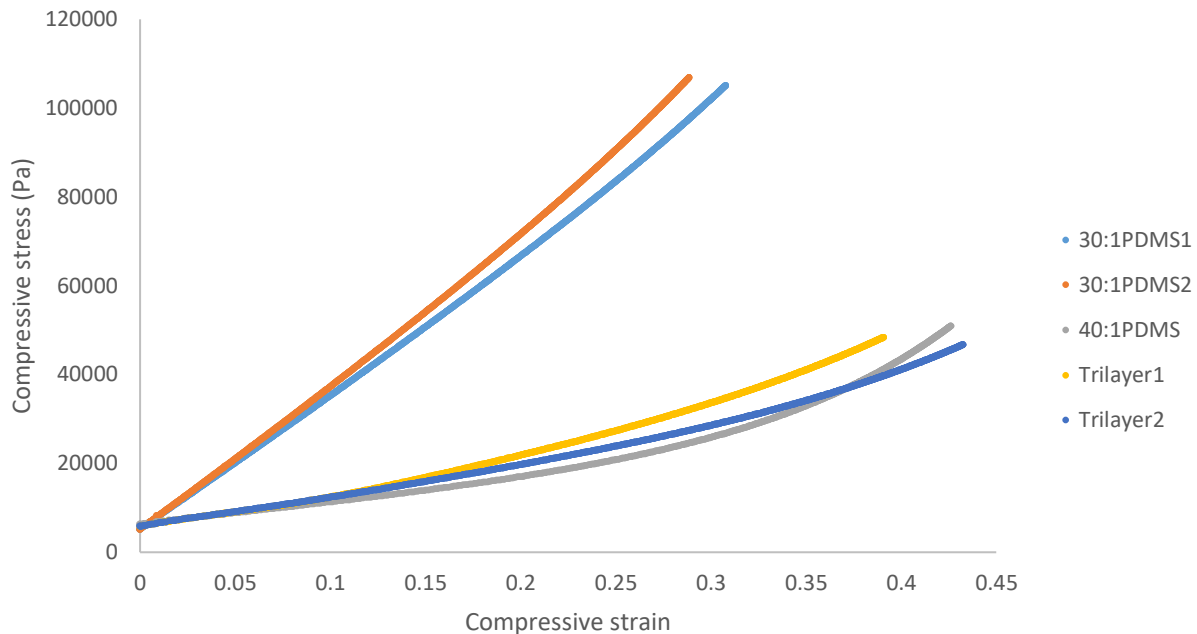| PDMS	Young's modulus (kPa)	R2 of fit for slope	Average thickness (mm)	Average diameter (mm)
30:1 PDMS1	299.78	1.000	3.89	9.56
30:1 PDMS2	321.08	0.9999	3.93	9.52
40:1 PDMS	49.25	0.9996	4.33	9.37
Trilayer 1	63.36	0.9986	3.01	9.59
Trilayer 2	63.81	0.9995	3.03	9.60

Figure S2: Stress-strain profiles for different materials tested, 1) 30:1 PDMS used for insertion experiments, 2) 40:1 PDMS, and 3) a tri-layer PDMS used to mimic 3 outer layers of the human skin.

Needle cutting and assembly

33G hypodermic needles (outer diameter: 203 µm; inner diameter: 89 µm) are used for experiments described here. One foot long stainless steel hypodermic tubing stocks (8988K84, McMaster-Carr) are cut to lengths of approximately 12 mm using a ceramic scoring wafer (Ceramic Scoring Wafer, Restek Corporation) by carefully scoring and breaking at the score line. The 12 mm needle segments and custom 3D printed Luer connectors (clear resin, Form 3 3D printer, Formlabs) are placed in a 3D printed assembly jig to control the target or exposed height of the needle to 6 mm (as shown in Fig. S1b and S1c). During assembly, uncured clear resin (Formlabs) is poured into the recess or reservoir of the Luer connectors (Fig. S1c), placed in a vacuum chamber to remove bubbles, and the poured resin is cured using ultraviolet (UV) illumination (Post-curing lamp, Kudo3D) to bond the needles to the Luer connectors. The UV curing is completed in two steps – firstly, the Luers stay in the jig (inverted position) for 30 minutes and then the needle-Luer assembly is removed from the jig and placed upright to complete the curing in 2-3 hours. After curing, the needles, with exposed heights of 6 mm, have their tips sanded on the ceramic wafer's flat surface and subsequently a 2000 grit sandpaper. The assembled devices are submerged in isopropyl alcohol (IPA) and sonicated for around 5 minutes to remove any debris.

Trilayer PDMS

A multi-layered PDMS is fabricated to mimic 3 layers of the human skin, using a similar technique described earlier[4,5]. The multi-layered PDMS is not transparent, and does therefore not allow for reliable puncture detection and determination of needle displacement, edge displacement, and needle inserted length.
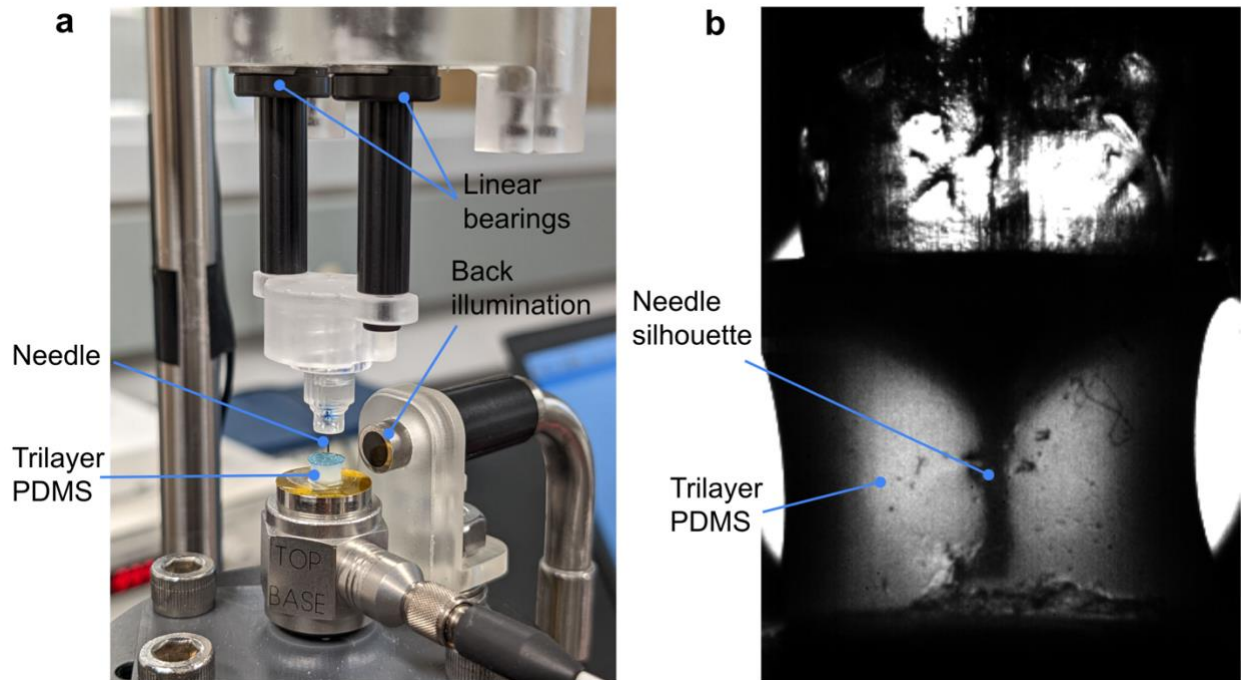
Figure S3: Insertion experiment with tri-layer PDMS, a) Experimental setup with linear bearings, with needle, PDMS and back illumination. b) Representative high-speed image of insertion, where puncture could not be identified by visual examination because the material was not fully transparent.

Experimental setup – dynamic insertion

The different components of the experimental setup[6] (shown in Fig. S4) are:

- *Imaging system*: The imaging system includes a high-speed camera, a telecentric lens and a ring light illuminator. The high-speed camera (Phantom Miro 4, Vision Research Inc.) with a 12 bit 800x600 SR-CMOS sensor has a pixel size of 22 μm. For the dynamic insertions, the frame rate is set to 7800 frames/second with a field of view of 208 pixels by 320 pixels (4.576 mm by 7.040 mm). A telecentric lens (1.0X - 3.0X VariMagTL™ Telecentric Lens, Edmund Optics Inc.) is attached to the high-speed camera to eliminate parallax/magnification errors. A ring light, powered by a halogen lamp (Steromaster Illuminator 12-562-6, Fisher Scientific), is attached to the telecentric lens to illuminate the soft solid sample and the needle assembly.
- *Translational stages*: A vertical (Z) translational stage (Compact Lab Jack, Thorlabs Inc.) under the camera adjusts the field of view (FOV) for the high-speed camera and another stage under the soft solid adjusts the relative position between the needle and the soft solid. A horizontal (Y) translational stage (DTS50, 2" Dovetail Translation Stage, Thorlabs Inc.) adjusts the FOV of the high-speed camera in that direction. Horizontal (X) translation to adjust the focus of the high-speed camera is implemented using two rail carriages (XT95P13 and XT95RC3, Thorlabs Inc.) that slide on a horizontal rail (XT95SP-500, Thorlabs Inc.).
- *Force sensor*: A piezoelectric force sensor (208C01, ICP Force sensor, PCB Piezotronics) is mounted, through a 3D printed adapter, to the vertical translational stage under the soft solid. The top part of the sensor includes an impact cap (084A03, PCB Piezotronics), on which a 2 mm thick stiff PDMS sample (made with 10:1 mixing ratio) rests to prevent damage to the sensor

and the 4 mm PDMS sample (made with 30:1 mixing ratio) used for insertion. By setting the analog gain of the data acquisition system (DAQ) to 10, the measurement range for the force was set to ±8.811 N and the force resolution measured by the DAQ was around 0.3 mN.

- *Vertical motion*: Two linear sleeve bearings (6673K11, High-Speed Linear Sleeve Bearing, McMaster-Carr) are mounted on a 3D printed housing that is fixed to the frame, while two linear motion shafts (1031K62, Linear Motion Shaft Ceramic-Coated 6061 Aluminum, McMaster-Carr) interface with the bearings. The shafts are cut to lengths of 45 mm and are attached to the moving assembly that includes the needle. Prior to using linear bearings, compliant mechanisms or flexures were also tested to prevent lateral motion (Fig. S5 in Supplementary information), but linear bearings were chosen for the final design because of their superior positional accuracy.
- *Moving assembly*: The moving assembly has a mass of around 20 grams and consists of a ferromagnetic disk (made of mild steel) at the top, two aluminum linear motion shafts, the needle-Luer assembly and 3-D printed connectors between these components.
- *Spring*: Compression of a 1 inch long spring (9002T467, McMaster-Carr) with a spring constant of 1677 N/m provides the impact energy of the needle and moving assembly. This spring provides impact velocities up to 4-5 m/s, and it could also be swapped for other stiffer springs if higher impact velocities are required.
- *Vertical positioning system*: An electromagnet (BDE-1212-12, Bunting Magnetics Co.) holds the ferromagnetic plate and the moving assembly in place after spring compression, and can release the moving assembly during the experiment. The electromagnet is mounted on a vertical position stand and can be positioned vertically in 1 mm increments (which corresponds to force increments of around 1.7 N and impact velocity increments of around 0.3 m/s).
- *Connections*: The piezoelectric force sensor is connected to a signal conditioner (482C05, PCB Piezotronics) and a data acquisition (DAQ) system (NI USB 6211, National Instruments Co.) that is connected to a laptop (Latitude 7490, Dell). The high-speed camera is connected to the laptop via an ethernet cable, and is also connected to the DAQ to enable synchronization of the high-speed imaging and the force measurements through software (Phantom Camera Control, Vision Research Inc.). The electromagnet is connected to a power supply via a double pole double throw (DPDT) switch, which enables reversing the polarity of the electromagnet to release the moving assembly.

Experimental procedure – dynamic insertion

The following procedure is followed for dynamic insertion and re-insertion experiments:

1. The soft solid sample (coated with carbon black and cut to a size of 10 mm by 10 mm) is placed on top of the piezoelectric force sensor and a conservative wait time of at least 5 minutes before insertion allows the force signal to decay and stabilize completely (discharge time constant of the force sensor is ≥50 sec).
2. The relative position of the needle tip and the soft solid surface is adjusted such that they are just in contact at the equilibrium position of the spring. Live imaging from the high-speed camera helps identify the position of contact.

3. With the electromagnet turned on, the moving assembly is moved upwards to contact the ferromagnetic disk with the electromagnet, which holds the moving assembly in place with the spring compressed at the preset compression length.
4. The high-speed camera is triggered and simultaneously, the DPDT switch is flipped to either turn the current off or to reverse the current polarity in the electromagnet, which releases the moving assembly and facilitates dynamic insertion of the needle into the soft solid.
5. For the re-insertion experiment, the moving assembly is moved upwards to remove the needle from the soft solid while the soft solid remains in the same position, and steps 3 and 4 are repeated after a 5 minute wait for the force signal to decay/stabilize.
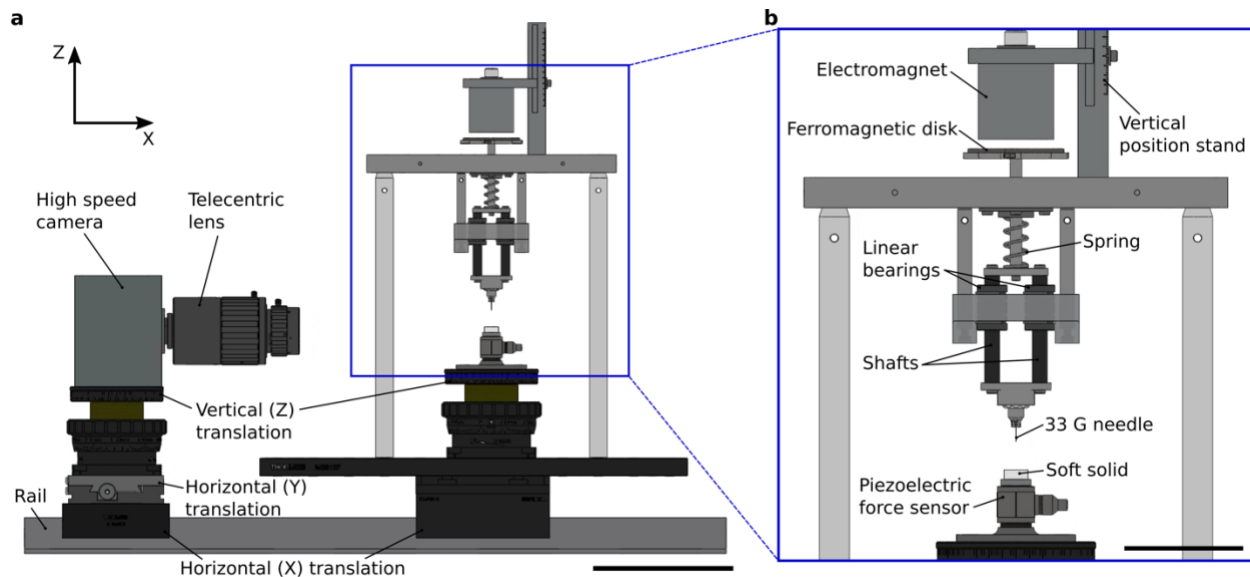

Figure S4 Experimental setup for dynamic insertion experiments: a) Imaging assembly (not showing the ring light), translational stages and the insertion apparatus; Scale bar is 100 mm. b) The ferromagnetic disk and the moving assembly are released when the current in the electromagnet is reversed or switched off, thus imparting the energy stored by the compression of the spring to the needle for dynamic insertions at velocities of up to 3-5 m/s; Scale bar is 50 mm.

Experimental setup – low-speed insertion

The experimental setup shown in Fig. S4 allows for dynamic insertion and re-insertion at velocities ranging from 0.2 m/s to 5 m/s. For lower insertion velocities, the needle is instead connected to a motorized linear stage (Zaber T-LSM050A, Zaber Technologies Inc.). The imaging system, translational stages and the base for the soft solid remain the same as for the setup for dynamic insertions. For low-speed insertions, the needle moves at prescribed velocities between 0.1 mm/s to 9 mm/s. In these experiments, a strain-gauge force sensor (LCM100-FSH04400, Futek Advanced Sensor Technology Inc.) provides the force measurements, and it is mounted between the needle-Luer assembly and the motorized linear stage (as shown in Fig. S1d). The strain-gauge force sensor and the motorized linear stage are connected to the laptop via USB connections.

Experimental procedure – low-speed insertion

The following procedure is followed for low-speed insertion and re-insertion experiments:

1. The soft solid sample (coated with carbon black and cut to a size of 10 mm by 10 mm) is placed on top of the piezoelectric force sensor and the force signal is allowed to decay and stabilize over at least 5 minutes. Here, even though the data analysis is performed only using measurements from the strain-gauge force sensor, forces are also measured with the piezoelectric force sensor as well to compare measurements between the two force sensors.
2. The needle is moved downwards (towards the soft solid) at a prescribed velocity of the motorized linear stage to a fixed distance, such that the needle stops before passing through the bottom surface of the sample.
3. The high-speed camera is triggered before contact of the needle with the solid surface, and the measurements of force (from the strain-gauge force sensor) and displacement (from the motorized linear stage) are recorded throughout the motion.
4. After the insertion experiment, the needle is removed from the soft solid by moving the motorized linear stage upwards, and steps 2 and 3 are repeated for the re-insertion experiment.

Design iterations for vertical motion

Flexure (3-segment)
- Frictionless
- Stiffness in Y ↓
- Stiffness in X ↑, Z ↑

Flexure (2-segment)
- Frictionless
- Stiffness in Y ↓
- Stiffness in X ↑, Z ~

Linear bearing
- Negligible friction
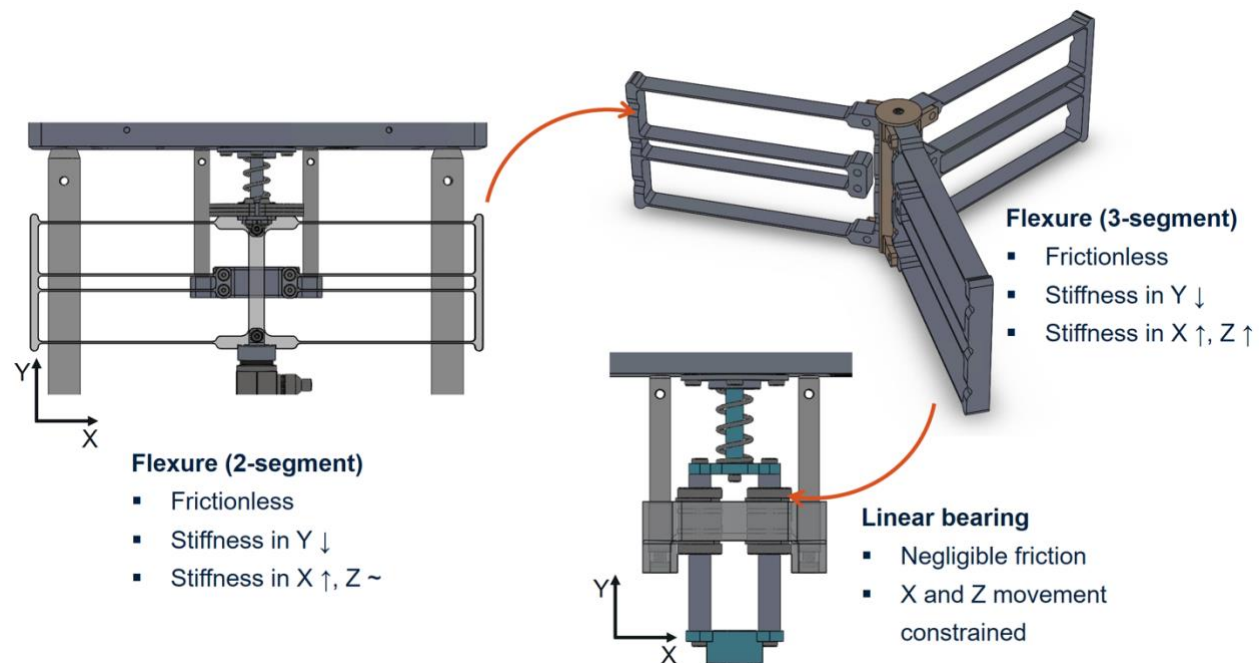- X and Z movement constrained

Figure S5: Different approaches for constraining vertical motion. Although theoretically frictionless, the compliant mechanisms or flexures using 2-segment and 3-segments did not produce positional accuracy of a few microns required for reliable double-insertion as did the linear bearing setup.
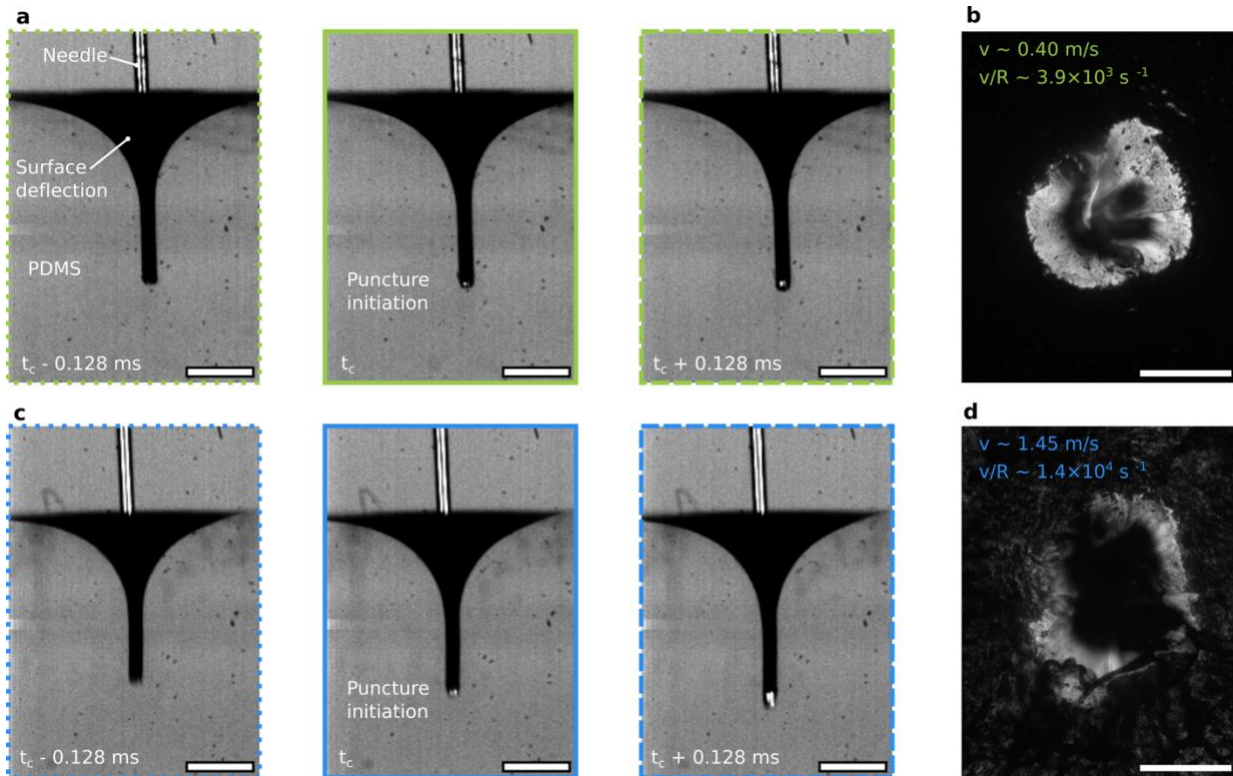
Puncture initiation detection images

Figure S6: a) Images of 3 successive frames around puncture initiation (puncture initiation detected in middle image) for insertion at 0.40 m/s (v/R ~ 3.9×103 s-1); tc = critical time, or time at puncture initiation. b) Microscopic image of crack formed after insertion at 0.40 m/s (v/R ~ 3.9×103 s-1). c) Images of 3 successive frames around puncture initiation for insertion at 1.45 m/s (v/R ~ 1.4×104 s-1). d) Microscopic image of crack formed after insertion at 1.45 m/s (v/R ~ 1.4×104 s-1). Scale bars in high-speed camera images (a and c) are 1 mm, and scale bars in microscope images of cracks (b and d) are 100 μm.

Crack size measurement

The circumference of the crack is measured after insertion/re-insertion experiments for 10 trials, as shown in Fig. S7, and the mean and standard deviation of the circumference of the crack is $C_{crack,top} = 604 \, \mu m \pm 35 \, \mu m$. The circumference is calculated for a fitted ellipse.
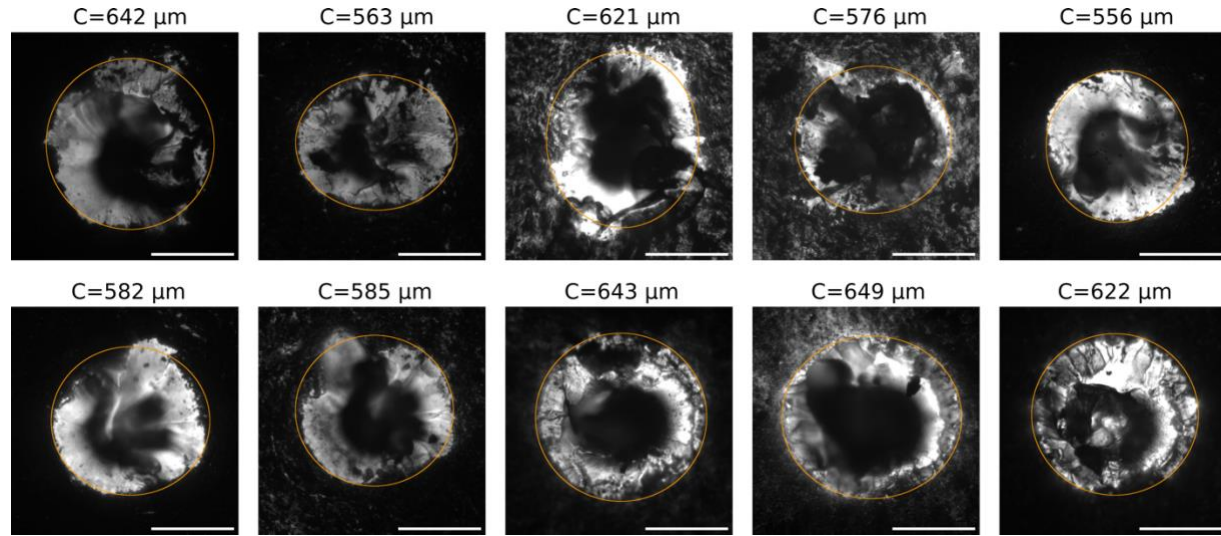
Figure S7: Images of the top surface of the crack for 10 experiments after insertion/re-insertion. The circumference of the fitted ellipse is stated above all images.

2D surface fitting for deformation force, velocity and displacement

Before puncturing the solid surface, the needle deforms the soft solid specimen and the specimen surface deflection increases with needle displacement. Consequently the measured force, equivalent to the deflection force F_d, increases non-linearly (Fig. S8a), as is also observed in other insertion experiments[7–9]. During the indentation stage (pre-puncture), the velocity of the needle stays relatively constant (Fig. S8a inset).

For calculating the deflection force using the proposed double-insertion method, F_d is modelled in the pre-puncture or indentation stage of the insertion experiment, where the measured force $F_{ins} = F_d$ and the needle displacement $d = d_e$, where d_e is the edge displacement or the vertical displacement of the solid surface. A 3D surface fit (Fig. S8b) of the form $F_d = A_1 d_e^{B_1} + A_2 v_e^{B_2} + A_3 d_e^{B_3} v_e^{B_4}$ agrees with 22 insertion experiments for 33G blunt needles, with an R^2 value of 0.9992 (other forms and coefficients for surface fits are shown in Fig. S9 and Tables S2-S5 in Supplementary information). The coefficients of the equation with 95% confidence bounds are $A_1 = 4.373 \times 10^7 \, Nm^{-B1} (4.256 \times 10^7 Nm^{-B1}, 4.490 \times 10^7 Nm^{-B1}), B_1 = 3.184 \ (3.180, 3.189), A_2 = -0.01979 \, Nm^{-B2} s^{B2} (-0.02008 \, Nm^{-B2} s^{B2}, -0.01951 \, Nm^{-B2} s^{B2}), B_2 = 1.408 \ (1.392, 1.423), A_3 = 1792 \, Nm^{-(B3+B4)} s^{B4} (1774 \, Nm^{-(B3+B4)} s^{B4}, 1811 \, Nm^{-(B3+B4)} s^{B4}), B_3 = 1.315 \ (1.313, 1.316), B_4 = 0.2283 \ (0.2279, 0.2286)$. This equation is used to estimate the deflection force F_d using the corresponding values of d_e (edge displacement) and v_e (edge velocity) for all the stages of insertion and re-insertion experiments.
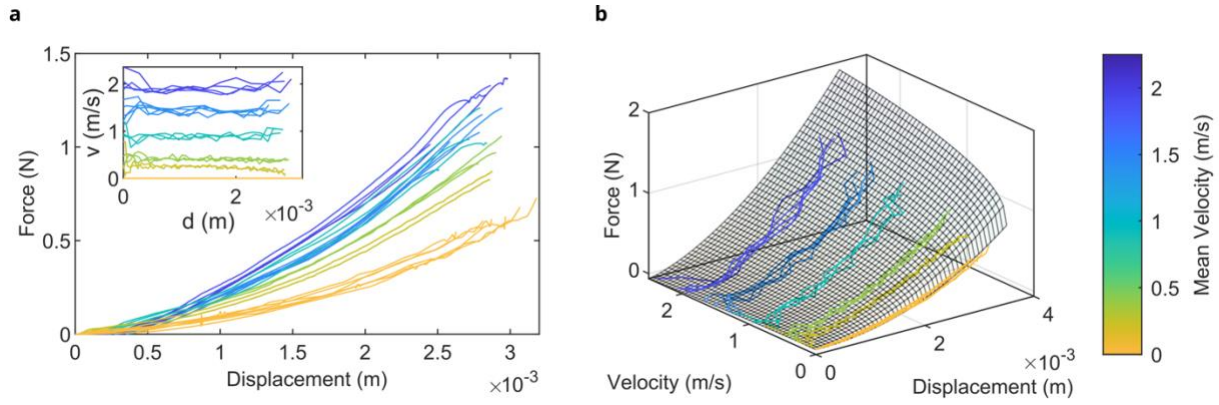
Figure S8 Indentation stage: a) Measured force (equivalent to deflection force F_d) during the insertion experiment before puncture increases non-linearly with increasing needle displacement (equivalent to edge displacement d_e). 22 sets of insertion experiments are shown with colors representing mean velocities pre-puncture. Inset: Needle velocity (v) during the indentation stage (d: needle displacement) stays relatively constant for the 22 insertion experiments. b) Surface fit of force as a function of needle displacement and velocity. Mean velocities range from 0.1 mm/s to 2.3 m/s (with R = 101.5 µm, and v/R ranging from 1 s^{-1} to 2.3 × 10^4 s^{-1}).

Different relationships between deformation force, velocity and displacement were tested.

$$F_d = A_1 d_e^{B_1} + A_2 v_e^{B_2} \qquad\qquad\qquad \text{(Fit1)}$$

$$F_d = A_1 d_e^{B_1} + A_2 v_e^{B_2} + A_3 d_e^{B_3} v_e^{B_4} \qquad\qquad\qquad \text{(Fit2)}$$

Table S2: Goodness of fit measures from MATLAB.

Fit	SSE	R^2
Fit1	532.1116	0.9114
Fit2	4.7376	0.9992

Sum of Squares Due to Error (SSE): Measures the total deviation of the data points from the fit in terms of the sum of squared errors, calculated as:

$$SSE = \sum_{i=1}^{n} (y_i - \hat{y_i})^2$$

where y_i is the value for the force at observation i, $\hat{y_i}$ is the predicted value for force at observation i.

R-square (R^2): It is the ratio of the sum of squares of the regression (SSR) and the total sum of squares (SST), where the different quantities are defined below.

$$SSR = \sum_{i=1}^{n} (\hat{y_i} - \bar{y})^2$$

$$SST = \sum_{i=1}^{n} (y_i - \bar{y})^2$$

$$R^2 = \frac{SSR}{SST} = 1 - \frac{SSE}{SST}$$

where y_i is the value for the force at observation i, $\hat{y_i}$ is the predicted value for force at observation i, and $\bar{y}$ is the mean.

Table S3: Summary of coefficients for the different fits

Fit	A_1	B_1	A_2	B_2	A_3	B_3	B_4
Fit1	7.797e+05 (7.415e+05, 8.18e+05)	2.349 (2.34, 2.357)	-6.722e-08 (-1.075e-06, 9.406e-07)	-1.527 (-3.155, 0.1007)	-	-	-
Fit2	4.373e+07 (4.256e+07, 4.49e+07)	3.184 (3.18, 3.189)	-0.01979 (-0.02008, -0.01951)	1.408 (1.392, 1.423)	1792 (1774, 1811)	1.315 (1.313, 1.316)	0.2283 (0.2279, 0.2286)

For Fit2, even though the coefficient A_2 is small relative to A_1 and A_3, since d_e and v_e are of orders of magnitude 10^{-3} m and 1 m/s, the first and second term are comparable. For instance, assuming $d_e = 10^{-3}$ m and $v_e = 1$ m/s, the values for the three terms are 0.01227 N, -0.01979 N and 0.2034 N. In this case, the first two terms are comparable and the third term dominates.

Table S4: Initial values and values after iterations for coefficients for the different fits for Fit1, with iterations with the lowest error and highest R² values in bold.

Fit1	A_1	B_1	A_2	B_2	SSE	R²
Iteration 1	0	0	0	0		
	1.679e+05 (1.589e+05, 1.77e+05)	2.082 (2.073, 2.091)	-0.006479 (-0.006863, -0.006094)	-0.3398 (-0.3469, -0.3327)	749.9254	0.8751
Iteration 2	1.679e+05	2.082	-0.006479	-0.3398		
	7.797e+05 (7.415e+05, 8.18e+05)	**2.349 (2.34, 2.357)**	**-6.722e-08 (-1.075e-06, 9.406e-07)**	**-1.527 (-3.155, 0.1007)**	**532.1116**	**0.9114**
Iteration 3	7.797e+05	2.349	-6.722e-08	-1.527		
	5.001e+05 (4.548e+05, 5.453e+05)	2.271 (2.256, 2.287)	-0.0006277 (-0.0008248, -0.0004307)	-0.554 (-0.5885, -0.5196)	1.8304e+03	0.6952

a

$$F_d = A_1 d_e^{B1} + A_2 v_e^{B2}$$

b

c

d

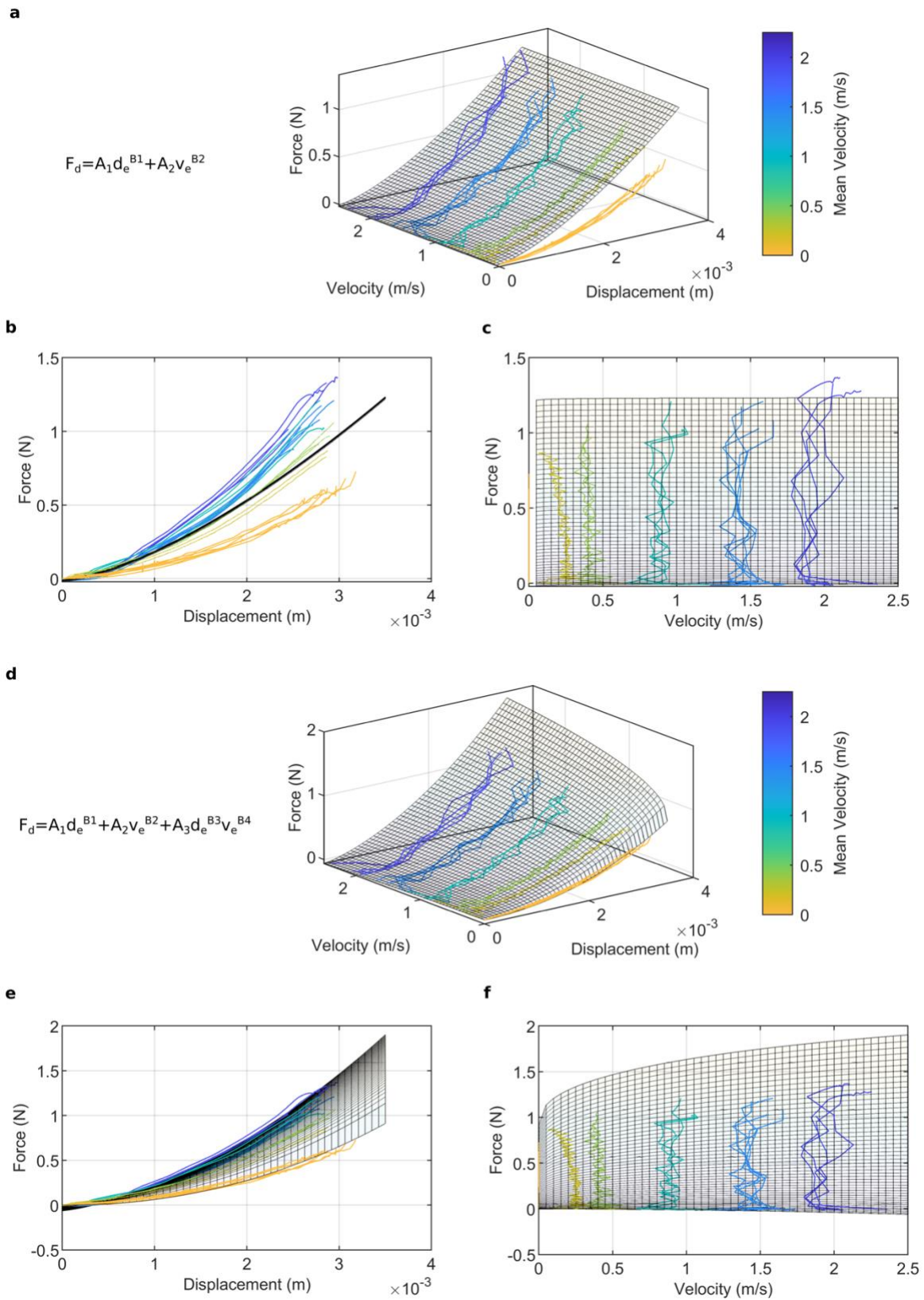$$F_d = A_1 d_e^{B1} + A_2 v_e^{B2} + A_3 d_e^{B3} v_e^{B4}$$

e

f

Figure S9: Surface fits for Fit1 and Fit2. a-c) Surface fit for 22 insertion experiments using Fit1. d-f) Surface fit for 22 insertion experiments using Fit2.

Table S5: Initial values and values after iterations for coefficients for the different fits for Fit2, with iterations with the lowest error and highest R^2 values in bold.

| Fit2	A_1	B_1	A_2	B_2	A_3	B_3	B_4	SSE	R^2
Iteration 1	0	0	0	0	0	0	0		
Limits	-100 to 100	-100 to 100	-100 to 100	-100 to 100	-100 to 100	-100 to 100	-100 to 100	824.3842	0.8627
	100 (81.46, 118.5)	1.001 (0.97, 1.032)	-0.1933 (-0.1993, -0.1873)	0.1904 (0.1824, 0.1983)	100 (88.94, 111.1)	0.8145 (0.7951, 0.834)	0.2878 (0.2835, 0.2921)		
Iteration 2	100	1.001	-0.1933	0.1904	100	0.8145	0.2878		
Limits	-1e+08 to 1e+08	-100 to 100	-1e+08 to 1e+08	-100 to 100	-1e+08 to 1e+08	-100 to 100	-100 to 100		
	8.526e+04 (8.009e+04, 9.043e+04)	2.113 (2.103, 2.123)	-0.01067 (-0.01167, -0.00968)	2.311 (2.186, 2.436)	2708 (2588, 2827)	1.401 (1.394, 1.409)	0.3018 (0.2997, 0.3039)	79.4886	0.9868
Iteration 3									
Limits	-1e+08 to 1e+08	-100 to 100	-1e+08 to 1e+08	-100 to 100	-1e+08 to 1e+08	-100 to 100	-100 to 100		
	1.969e+06 (1.888e+06, 2.051e+06)	2.615 (2.608, 2.622)	-0.01994 (-0.02073, -0.01915)	1.851 (1.802, 1.9)	1332 (1294, 1370)	1.284 (1.279, 1.288)	0.2937 (0.2924, 0.2951)	36.4951	0.9939
Iteration 4									
Limits	-1e+08 to 1e+08	-100 to 100	-1e+08 to 1e+08	-100 to 100	-1e+08 to 1e+08	-100 to 100	-100 to 100		
	1.551e+07 (1.495e+07, 1.607e+07)	2.975 (2.969, 2.982)	-0.02547 (-0.02603, -0.0249)	1.392 (1.369, 1.416)	1015 (995.6, 1034)	1.231 (1.228, 1.234)	0.2612 (0.2604, 0.2621)	16.6345	0.9972
Iteration 5	1.551e+07	2.975	-0.02547	1.392	1015	1.231	0.2612		
	-1e+09 to 1e+09	-100 to 100	-1e+09 to 1e+09	-100 to 100	-1e+09 to 1e+09	-100 to 100	-100 to 100		
	4.373e+07 (4.256e+07, 4.49e+07)	**3.184 (3.18, 3.189)**	**-0.01979 (-0.02008, -0.01951)**	**1.408 (1.392, 1.423)**	**1792 (1774, 1811)**	**1.315 (1.313, 1.316)**	**0.2283 (0.2279, 0.2286)**	**4.7376**	**0.9992**
Iteration 6	4.373e+07	3.184	-0.01979	1.408	1792	1.315	0.2283		
	-1e+09 to 1e+09	-100 to 100	-1e+09 to 1e+09	-100 to 100	-1e+09 to 1e+09	-100 to 100	-100 to 100		
	3.855e+07 (3.751e+07, 3.96e+07)	3.149 (3.144, 3.153)	-0.02223 (-0.02256, -0.02189)	1.349 (1.334, 1.365)	1380 (1364, 1396)	1.276 (1.274, 1.278)	0.2375 (0.237, 0.2379)	6.2161	0.9990

Friction and spreading force
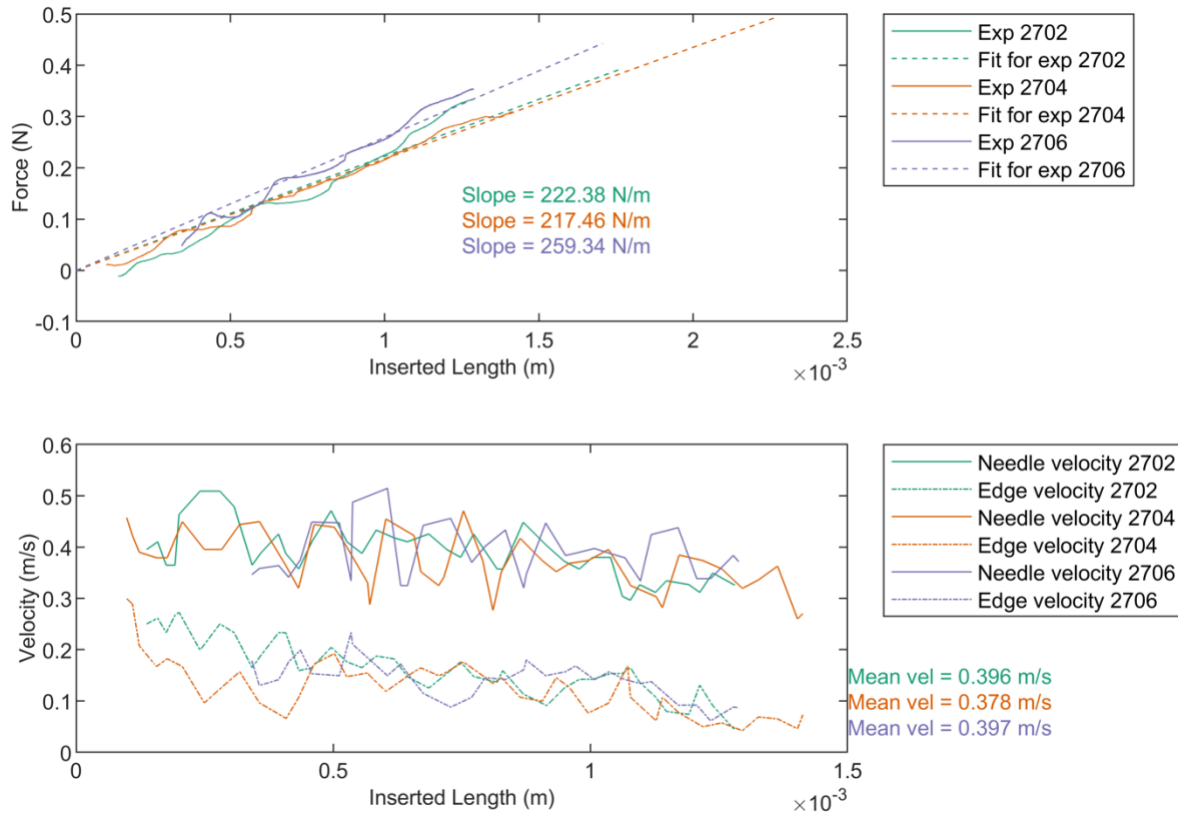
Figure S10: Top: Linear fit of friction and spreading force $F_f + F_s = F_{m,re-ins} - F_d$ as a function of inserted length for 3 re-insertion experiments. Bottom: Needle velocities (solid lines) and edge velocities (dashed lines) for the region where frictional force and spreading force were modeled for the three experiments, showing that velocity stays relatively constant.
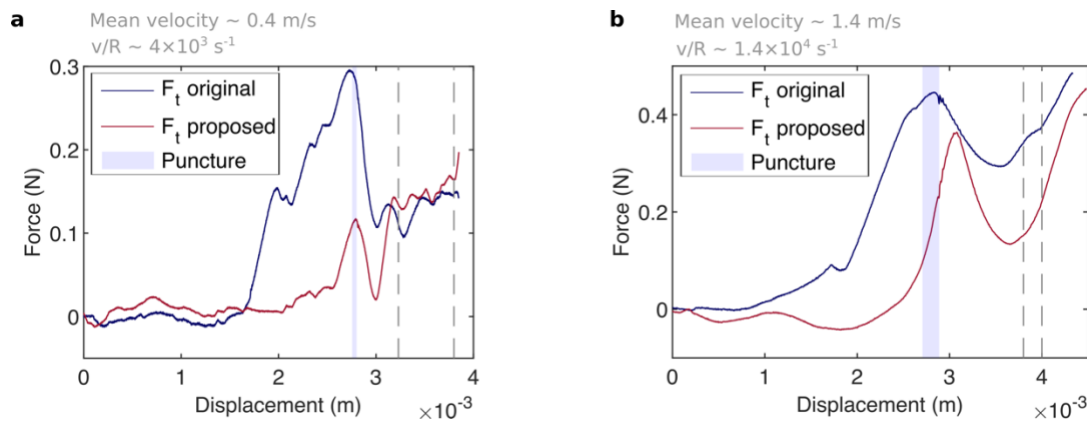
Cutting force

Figure S11: Comparison of cutting force for original (blue; $F_t = F_{ins} - F_{reins}$) and proposed (maroon; $F_t = F_{ins} - F_d - F_f - F_s$) double-insertion method for mean velocity of 0.4 m/s (a) and 1.4 m/s (b).
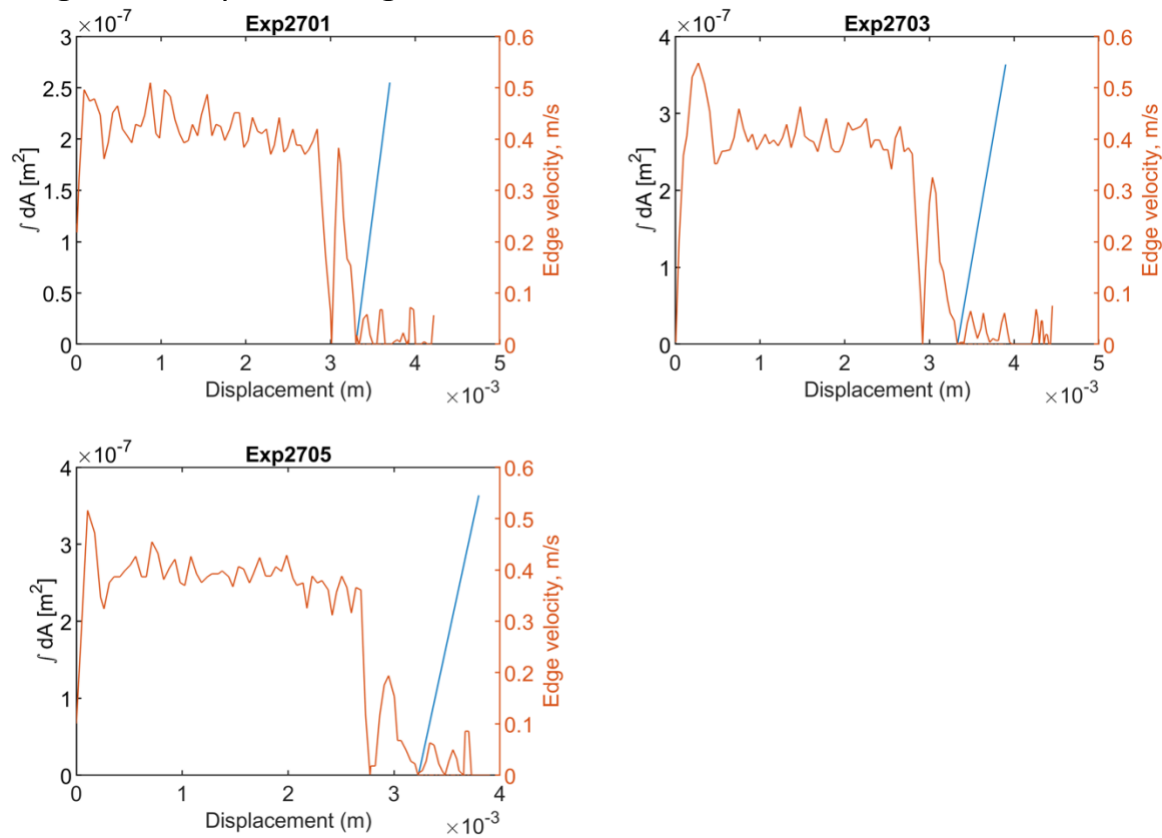
Edge velocity and toughness calculation

Figure S12: Edge velocity (orange) and crack area (blue) used to calculate toughness for three insertion experiments, shows that the toughness was calculated in the region when edge velocity decreases and stabilizes - indicating a more stable cutting stage than during initial puncture, which corresponds to the moment when edge velocity suddenly decreases (around or before 3 mm).

Extended double insertion method

The main differences between the original and our proposed double-insertion methods are provided in Table S6.

Table S6: Comparison of original and extended double-insertion methods

	Original double-insertion method	**Extended double-insertion method**
Primary measurements	Force F, displacement d or imaging	Force F, Imaging
Secondary measurements	d (if imaging used), v	d, d_e, d_{il}, v, and v_e
Force components determined	F_t	F_d, F_f, F_s, and F_t
Equation for cutting force	$F_t = F_{m,ins} - F_{m,reins}$	$F_t = F_{m,ins} - F_d - F_f - F_s$
Cutting force pre-puncture	Non-zero pre-puncture	Close to zero pre-puncture
Deformation, friction and spreading	Assumes same deformation and inserted needle length (and thus same F_d, F_f, and F_s) between insertion and re-insertion	Assumes different deformation and inserted needle length; F_d and $F_f + F_s$ are calculated separately (Fig. 4)
Needle sharpness	Mostly been applied to sharp needles (with low bevel angles)	Applied to blunt needles (and can be extended to sharp needles)
Insertion speed	Tested for quasi-static insertions with speeds up to 0.08 m/s[8,10–12]	Tested for wide range of speeds: 10^{-4} m/s to 2.5 m/s

Inertial energy sample calculation

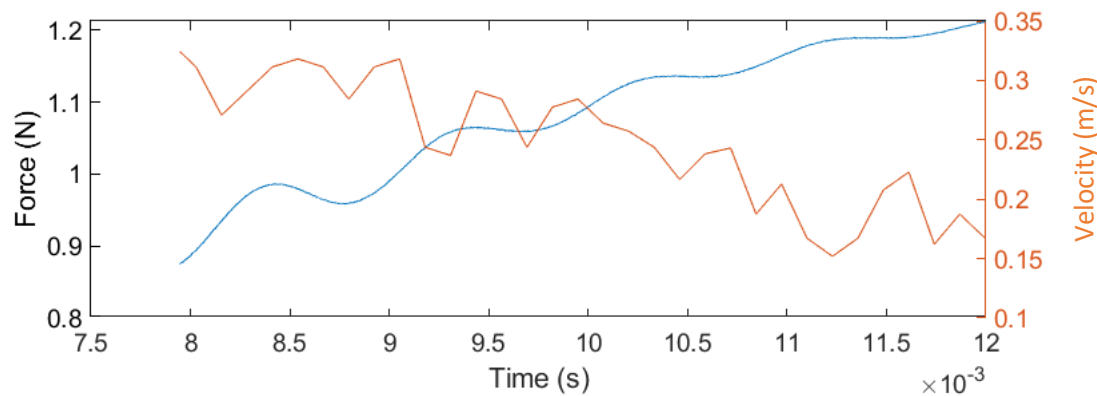Figures S13 and S14 show the forces and velocities during cutting phase of one insertion experiment.

Figure S13: Force vs. time (blue) and velocity vs. time (orange) after puncture initiation (insertion experiment)
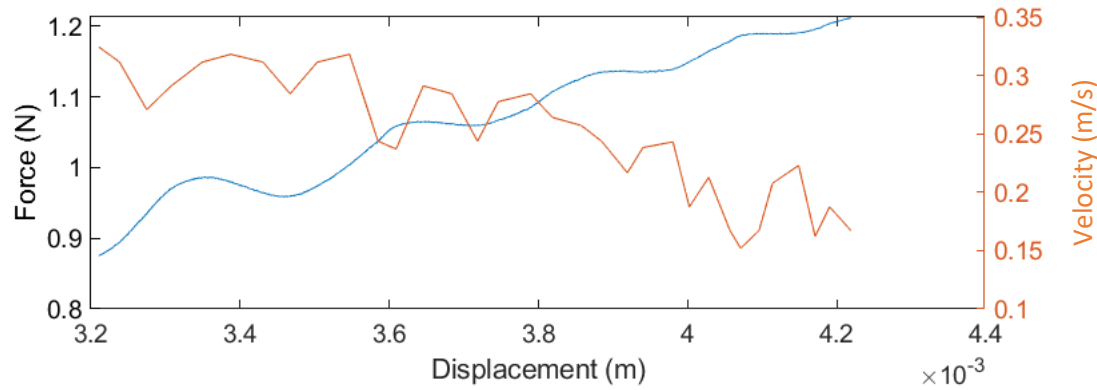
Figure S14: Force vs. displacement (blue) and velocity vs. displacement (orange) after puncture initiation (insertion experiment)

The velocity decreases as a function of time or displacement during the cutting phase, which results in a decrease in the inertial energy. Table S8 show the initial and final values in the plots (Figs S13 and S14).

Table S8: Initial and final values for velocity, time, displacement and force

	Initial	Final	Difference or average*
Velocity	$v_i = 0.32437 \; m/s$	$v_f = 0.16718 \; m/s$	$\Delta v = -0.15719 \; m/s$
Time	$t_i = 0.0079462 \; s$	$t_f = 0.011996 \; s$	$\Delta t = 0.0040499 \; s$
Displacement	$d_i = 0.0032105 \; m$	$d_f = 0.0042189 \; m$	$\Delta d = 0.0010084 \; m$
Force*	$F_i = 0.87514 \; N$	$F_f = 1.2128 \; N$	$F_{avg} = 1.044N$

* Average calculated for force, while difference calculated for rest

Work done by the needle

The work done by the needle is the sum of energies for deformation, friction, spreading and cutting.

Work done by needle, calculated as area under force displacement curve during cutting phase, or area under blue curve in Fig. S13 or S14 (calculated using '*trapz*' function in MATLAB).

$$W_{needle} = 0.0010758 \; Nm$$

Note: This estimate is similar to the estimate using average force F_{avg} multiplied by difference in displacement Δd because the force is approximately linear

$$W_{needle,avg} = F_{avg}\Delta d = 1.044N \times 0.0010084m = 0.0010527 \; Nm$$

Inertial energy

Average acceleration is estimated using

$$a_{avg} = \frac{\Delta v}{\Delta t} = \frac{-0.15719 \; m/s}{0.0040499 \; s} = -38.8133 \; m/s^2$$

Average inertial force during the cutting force

$$F_{avg,inertial} = m \times a_{avg} = 0.02 \ kg \ \times -38.8133 \ m/s^2 = -0.7763 \ N$$

Inertial energy lost during needle insertion

$$E_{inertial} = F_{avg,inertial} \times \Delta d = -0.7763 \ N \times 0.0010084 m = -0.0007827 \ Nm$$

Note: This estimate of inertial energy is similar to $\frac{1}{2} m \left(v_f^2 - v_i^2 \right) = -0.0007727 \ Nm$

Based on this estimate, the estimate of inertial energy lost (0.78 mJ) is similar to the estimate of work done by the needle (1 mJ) during the cutting phase.

Table S9: Estimates for energies other 4 experiments.

	W_{needle}	$W_{needle,avg}$	$E_{inertial}$
2701 (above)	1.08 mJ	1.05 mJ	-0.78 mJ
2703	1.34 mJ	1.28 mJ	-1.27 mJ
2705	0.88 mJ	0.87 mJ	-0.80 mJ
2201	1.42 mJ	1.40 mJ	-1.21 mJ

The inertial energy lost (calculated using the mass and acceleration of the needle assembly) is similar to the work done by the needle (calculated using measured force and needle displacement).

Toughness

Figure S15 compares the values of toughness obtained in this study with data reported by other researchers using the double-insertion method for synthetic materials and biological tissue. The same data presented in Figure 8c are shown in Figure S15, but with velocity on the x-axis instead of strain rate.
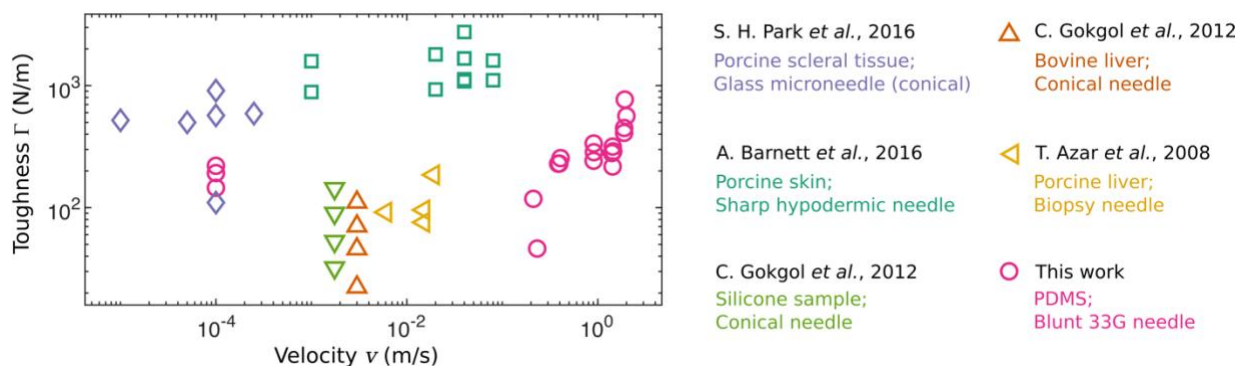

Figure S15: Comparison of toughness Γ estimated for different biological and synthetic materials determined by the double-insertion method using different types of needles[8,10–12], as a function of needle velocity.

Toughness estimation with pure shear tests

The toughness of the PDMS samples is verified through an alternative method to validate the method presented in this manuscript. This pure shear test uses the load-displacement behavior of specimens with and without a notch.

Materials and methods for the toughness estimation with pure shear tests

The PDMS specimen employed in this pure shear test are from the exact same fabrication run as the samples used in the double insertion experiments. This avoids uncertainties in mechanical properties of PDMS that can vary with the manufacturing batch of the supplier and with the exact mixing and curing protocols. The samples are approximately 8-10 mm wide and 4.5 mm thick. A notch is created in some of the samples; a CO_2 laser slightly scores the surface of these samples by 4.5 mm from one edge to facilitate placing a straight cut across the samples using a razor blade. Table S10 and Table S11 show the dimensions of the pristine and the notched samples, respectively, where the width corresponds to the original width reduced by the length of the notch.

Table S10: Dimensions of the pristine PDMS samples for pure-shear testing

Specimen	S_1	S_2	S_3	average
Width (mm)	9.4	8.6	9.6	9.2
Thickness (mm)	4.7	4.6	4.1	4.47

Table S11: Dimensions of the notched PDMS samples for pure-shear testing

Specimen	S_{n1}	S_{n2}	S_{n3}	average
Width (mm)	4.1	3.6	3.4	3.7
Thickness (mm)	4.6	4.2	4.8	4.6

Each specimen is characterized with an Instron 5969 uniaxial tester equipped with a 50 N load cell. Grips clamp the specimen along its width with an initial distance between grips of $l = 2.3$ mm at zero load. The notch of the non-pristine specimens is located about the same distance from either grip, to preserve the symmetry of the pure-shear model system. The specimen is stretched at 2 mm/minute by about 4 mm (total test duration 2 minutes) and, in the case of the notched specimens, until they fail. Load F and displacement d are recorded at 10 Hz. With the velocity of 2mm/minute and original sample height of 2.3 mm, the estimated strain rate is $1.4 \times 10^{-2} s^{-1}$.

Toughness calculation

Fig. S16 shows the plot of engineering (1st Piola-Kirchhoff) stress t versus stretch λ for three PDMS pristine sample (S_1, S_2, S_3) and three notched samples (S_{n1}, S_{n2}, S_{n3}) pulled along the direction of stretch λ, under pure shear conditions. We have then

$$t = \frac{F}{A_0} \tag{1}$$

with A_0 the initial specimen area, as well as

$$\lambda = 1 + \frac{d}{l} \tag{2}$$

The average width $w = 9.2 \ mm$, for pristine samples, and $w = 3.7 \ mm$ for notched samples, with average thickness $t = 4.47 \ mm$ for pristine samples and $t = 4.6 \ mm$ for notched samples. These quantities yield an initial area $A_0 = w \ t = 41.12 \ mm^2$ for pristine samples, and $17.02 \ mm^2$ for notched samples.
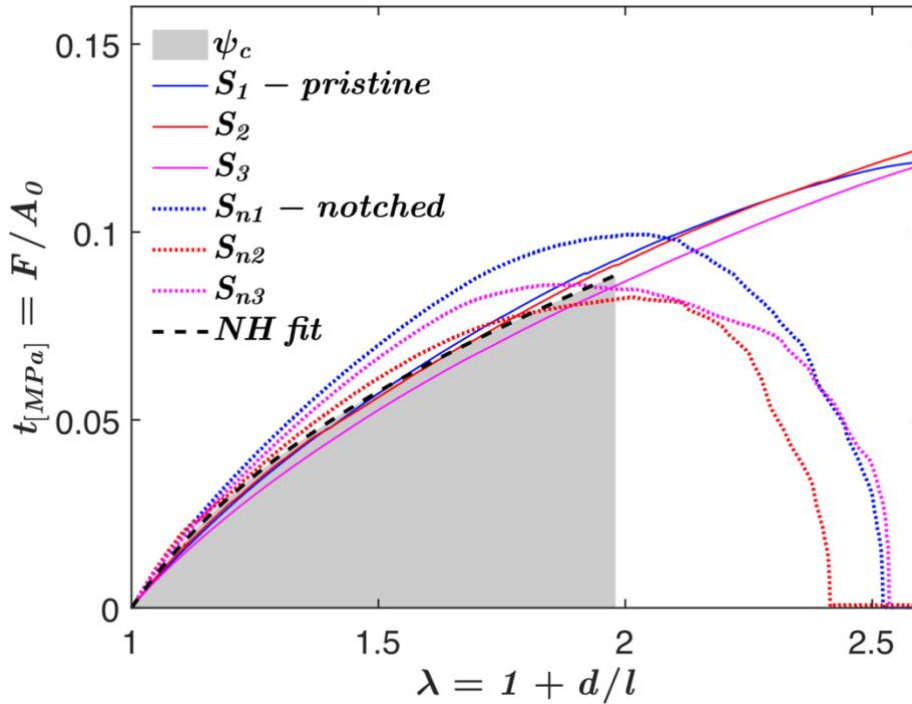

Figure S16 – Engineering (1st Piola-Kirchhoff) stress t, in MPa, versus stretch λ for experiments on pristine samples (solid lines) versus incompressible neo-Hookean (NH) fit assuming a shear modulus $\mu = 47.8 \ kPa$ (black line). Grey shading indicates the critical work of rupture W_c up to the critical stretch $\lambda_c = 2.48$ at which the notched samples fail.

Consider a neo-Hookean incompressible material, with strain energy density in the undeformed state

$$\psi = \frac{\mu}{2}(\lambda_1^2 + \lambda_2^2 + \lambda_3^2 - 3). \tag{3}$$

Under the assumption of plane strain deformation, substantiated by sample thickness being larger than length (4.47 mm versus 2.3 mm), we can assume $\lambda_3 = 1$. Incompressibility then imposes $J = \lambda_1 \lambda_2 = 1$, giving

$$\lambda_2 = \frac{1}{\lambda_1} \tag{4}$$

which, substituted in Eq. (3), taking $\lambda_1 = \lambda$ yields

$$\psi = \frac{\mu}{2}(\lambda^2 + \lambda^{-2} - 2). \tag{5}$$

Now, the engineering stress becomes

$$t = \frac{\partial \psi}{\partial \lambda} = \mu(\lambda - \lambda^{-3}) \tag{6}$$

which, fitted to the experimental data in Fig. S16 results in a shear modulus $\mu = 47.8\ kPa$, with an $R^2 = 0.99$ for the range $1 \leq \lambda \leq 2.5$.

The critical stretch $\lambda_c = \frac{2.05+2.02+1.86}{3} = 1.98$ corresponds to the average stretch at maximum engineering stress in Fig. S16. Substituting this, with the estimated shear modulus, in Eq. (5) we have $\psi_c = 52.0\ kPa$. By multiplying ψ_c by the sample length l we obtain the toughness of the material as $\Gamma = \psi_c l = 119.6\ N/m$.

References

1   Y. Xia and G. M. Whitesides, *Annu. Rev. Mater. Sci.*, 1998, **28**, 153–184.

2   T. Fujii, *Microelectron. Eng.*, 2002, **61**–**62**, 907–914.

3   J. C. McDonald and G. M. Whitesides, *Acc. Chem. Res.*, 2002, **35**, 491–499.

4   S. A. Ranamukhaarachchi, T. Schneider, S. Lehnert, L. Sprenger, J. R. Campbell, I. Mansoor, J. C. Y. Lai, K. Rai, J. Dutz, U. O. Häfeli and B. Stoeber, *Macromol. Mater. Eng.*, 2016, **301**, 306–314.

5   S. A. Ranamukhaarachchi and B. Stoeber, *Biomed. Microdevices*, 2019, **21**, 1–8.

6   P. Shrestha, C. Geffner, M. Jaffey, Z. Wu, M. Iapichino and B. Stoeber, 2024.

7   D. J. van Gerwen, J. Dankelman and J. J. van den Dobbelsteen, *Med. Eng. Phys.*, 2012, **34**, 665–680.

8   A. C. Barnett, Y.-S. Lee and J. Z. Moore, *J. Manuf. Sci. Eng.*, 2016, **138**, 011005.

9   S. Fakhouri, S. B. Hutchens and A. J. Crosby, *Soft Matter*, 2015, **11**, 4723–4730.

10   S. H. Park, K. J. Lee, J. Lee, J. H. Yoon, D. H. Jo, J. H. Kim, K. Kang and W. Ryu, *Acta Biomater.*, 2016, **44**, 286–294.

11   C. Gokgol, C. Basdogan and D. Canadinc, *Med. Eng. Phys.*, 2012, **34**, 882–891.

12   T. Azar and V. Hayward, in *Biomedical Simulation*, Springer Berlin Heidelberg, Berlin, Heidelberg, 2008, vol. 5104, pp. 166–175.